Remote Sensing of Environment 185 (2016) 84–94

Contents lists available at ScienceDirect

Remote Sensing of Environment

journal homepage: www.elsevier.com/locate/rse

Rapid large-area mapping of ice flow using Landsat 8

Mark Fahnestock [a,*], Ted Scambos [b,*], Twila Moon [b,c], Alex Gardner [d], Terry Haran [b], Marin Klinger [b]

[a] Geophysical Institute, University of Alaska Fairbanks, Fairbanks, AK 99775, USA
[b] National Snow and Ice Data Center (NSIDC), University of Colorado at Boulder, Boulder, CO 80303, USA
[c] Department of Geological Sciences, University of Oregon, Eugene, OR 97403, USA
[d] Jet Propulsion Laboratory, California Institute of Technology, Pasadena, CA 91109, USA

ARTICLE INFO

Article history:
Received 22 July 2015
Received in revised form 4 November 2015
Accepted 14 November 2015
Available online 25 November 2015

Keywords:
Landsat
Ice flow
Greenland
Antarctica
Remote sensing
Glaciers

ABSTRACT

We report on the maturation of optical satellite-image-based ice velocity mapping over the ice sheets and large glacierized areas, enabled by the high radiometric resolution and internal geometric accuracy of Landsat 8's Operational Land Imager (OLI). Detailed large-area single-season mosaics and time-series maps of ice flow were created using data spanning June 2013 to June 2015. The 12-bit radiometric quantization and 15-m pixel scale resolution of OLI band 8 enable displacement tracking of subtle snow-drift patterns on ice sheet surfaces at ~1 m precision. Ice sheet and snowfield snow-drift features persist for typically 16 to 64 days, and up to 432 days, depending primarily on snow accumulation rates. This results in spatially continuous mapping of ice flow, extending the mapping capability beyond crevassed areas. Our method uses image chip cross-correlation and sub-pixel peak-fitting in matching Landsat path/row pairs. High-pass filtering is applied to the imagery to enhance local surface texture. The current high image acquisition rates of Landsat 8 (725 scenes per day globally) reduces the impact of high cloudiness in polar and mountain terrain and allows rapid compilation of large areas, or dense temporal coverage of seasonal ice flow variations. The results rival the coverage and accuracy of interferometric Synthetic Aperture Radar (InSAR) mapping.

1. Background

Feature tracking, in its early application for ice flow determination, was applied to oblique time-lapse photographs or repeat aerial photography, and involved manual identification of the same features in two images, displaced over the image pair interval by ice flow (e.g. Harrison, Echelmeyer, Cosgrove, & Raymond, 1992; Krimmel, 1987; Whillans & Bindschadler, 1988). Feature tracking expanded ice flow measurement beyond repeated geodetic surveys of markers on the ice, and allowed intermediate measurements during long intervals between field seasons. Efforts to follow displacement of features in satellite images started with similar techniques (e.g. Lindstrom & Tyler, 1984; Lucchitta & Ferguson, 1986), but tools were soon developed that exploited the digital nature of the imagery.

The advent of moderate-resolution imaging of the earth surface from space by Landsat led to the development of satellite-image-based tracking of ice sheet flow over twenty-five years ago. A major early advance was the development of computerized correlation algorithms and digital enhancement of the images (Bindschadler & Scambos, 1991; Emery, Fowler, Hawkins, & Preller, 1991; Scambos, Dutkiewicz, Wilson, & Bindschadler, 1992). The first significant areas mapped using computational methods were the broad ice streams flowing into the Ross Ice Shelf and regions of the Larsen Ice Shelf, both in Antarctica, where large crevasses could be followed in ~30 m resolution Thematic Mapper imagery from Landsat 4 and 5 (Bindschadler, Fahnestock, Skvarca, & Scambos, 1994; Bindschadler, Vornberger, Blankenship, Scambos, & Jacobel, 1996; Scambos, Echelmeyer, Fahnestock, & Bindschadler, 1994). Similar techniques were later applied to map surface displacements of smaller mountain glacier systems (e.g. Berthier et al., 2005; Kääb, 2002). Computer-based tracking of the long curvilinear crevasses common in these areas substantially increased knowledge of ice flow patterns compared to field-based techniques. Subsequently, imaging radars allowed wide-area ice flow mapping based on satellite-borne synthetic aperture radar (SAR) coverage, using both speckle tracking (similar to feature tracking in visible-band images) and interferometric determination of ice displacement (InSAR; Frolich & Doake, 1998). Radar coverage did not suffer from cloud obscuration of the surface, and had a strong textural response over both crevassed and uncrevassed areas due to unique speckle or phase-based signatures in the radar energy reflection from ice sheet surface and sub-surface structures. This again revolutionized our knowledge of large ice sheet flow patterns, leading to the first comprehensive ice flow maps at the ice sheet scale (e.g., Jezek, 2008; Joughin, Smith, Howat, Scambos, & Moon, 2010; Rignot, Mouginot, & Scheuchl, 2011).

* Corresponding authors.
E-mail addresses: mark.fahnestock@mac.com (M. Fahnestock), teds@nsidc.org (T. Scambos).

http://dx.doi.org/10.1016/j.rse.2015.11.023

In these early applications, a limitation common to Landsat and other visible-band satellite image data sets with limited radiometric resolution over bright targets was that feature tracking required high-contrast surface features (crevassed areas), leading to patchy ice velocity retrievals. Image acquisitions were infrequent (typically 0 to 4 acquisitions per year for a scene center in the 1990s) and cloudiness in the polar regions further reduced usable coverage. Poor image geolocation and internal geometric distortion often meant extensive pre-processing to co-register image pairs prior to ice flow data extraction. The Advanced Spaceborne Thermal Emission and Reflection Radiometer (ASTER) and Landsat 7, both launched in 1999, improved most aspects of ice flow mapping from visible-band satellite data, with better spatial resolution (10 and 15 m, respectively), improved acquisition rate, and better geolocation and image geometry. This has been widely applied to individual glaciers or small glacierized regions (e.g., Berthier, Arnaud, Baratoux, Vincent, & Rémy, 2004). However, large-scale ice sheet velocity mapping was still impractical because of low acquisition rates and because the dynamic range of the sensors, once distributed across dark (e.g. ocean) and highly reflective (snow and ice) targets, contained limited radiometric information over ice.

Improvements in radiometric resolution, geolocation accuracy, and image acquisition rates for Landsat 8, launched in 2013, allow us to overcome these limitations and provide velocity mapping on an ice-sheet-wide scale, or over an entire glacierized region, on a frequent basis. Landsat 8 has maintained a high acquisition rate, currently capturing ~725 images per day over the 16-day orbit repeat cycle, leading to excellent image coverage (Fig. 1). With 12-bit radiometric quantization, compared to the 8 bits per channel in earlier instruments, Landsat 8 can track subtle contrast variations over bright targets, such as sastrugi (snow dunes at ~five meter scale). This capability was first demonstrated with the Advanced Land Imager (ALI) on EO-1, a precursor to the Landsat 8 Operational Land Imager (OLI) (Bindschadler, 2003). OLI panchromatic band imagery has nearly an order of magnitude better signal to noise ratio than Landsat 7 ETM+, and much less saturation for bright targets (Morfitt et al., 2015). This, combined with ~half-pixel geolocation accuracy and high spatiotemporal data acquisition rates, enables ice velocity measurements having a quality and quantity not previously achievable with visible-band satellite imagery. Furthermore, the software presented here (*Py*thon image *Corr*elation or PyCorr) and ongoing improvements in accessibility and geolocation of the USGS Landsat 7 archive (www.earthexplorer.usgs.gov) are facilitating improved, though not ice-sheet-wide, ice velocity mapping using Landsat 7.

2. Methods

2.1. Large area mapping via automated surface feature tracking

To map ice flow, small image subscenes, or 'chips', containing features from one image, are compared to a range of possible matching locations in a second image, with the best match determined by generating a normalized cross-correlation surface composed of the cross-correlations of the chips at each integer pixel offset in that range. Mathematical interpolation of the primary peak in this surface allows determination of feature offset at the sub-pixel level. The earliest available software that incorporated this process with a view toward tracking of surface feature movement, and made it available outside of large image processing packages, was IMCORR (nsidc.org/data/velmap/imcorr.html; Fahnestock, Scambos, & Bindschadler, 1992). A number of later implementations of this technique have been developed, beginning with Whillans and Tseng (1995). Several recent approaches are compared in Heid and Kääb (2012); differences between implementations involve approaches to image resampling, filtering and peak fitting, strategies for identifying incorrect offsets ("bad matches") (e.g. Ahn & Howat, 2011), simultaneous estimation of strain and rotation as well as displacement (eg. Debella-Gilo &

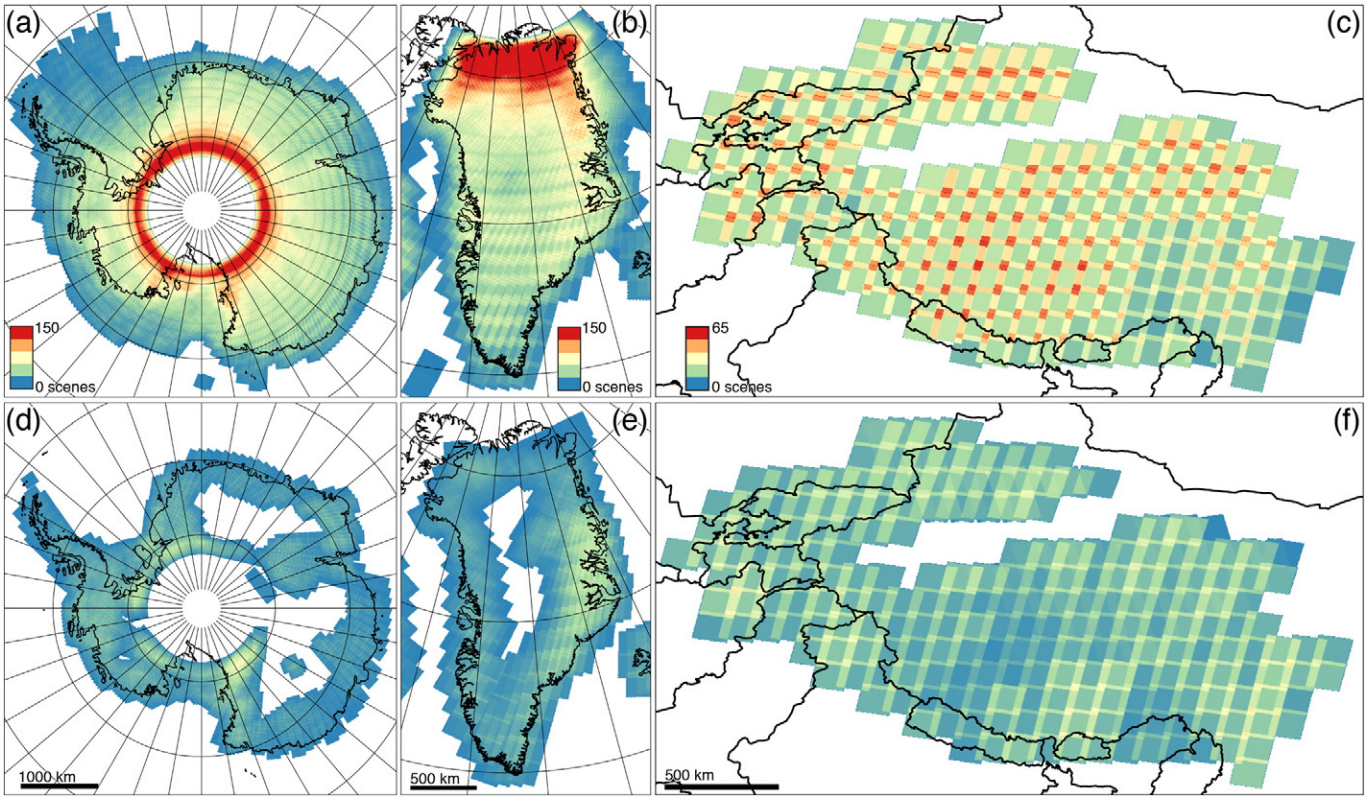

Fig. 1. Maps of Landsat 8 image coverage in a) Antarctica (1 Oct. 2014–31 Mar. 2015); b) Greenland (1 Mar.–31 Oct. 2014); and c) central Asia (1 Mar.–31 Oct. 2014); and Landsat 7 image coverage in d) Antarctica (1 Oct. 2012–31 Mar. 2013), e) Greenland (1 Mar.–31 Oct. 2012), and f) central Asia (1 Mar.–31 Oct. 2012). Images included have a 5° sun elevation cutoff and ≤50% cloud cover.

Kääb, 2012; Whillans & Tseng, 1995), and methods to correct for geometric distortion during image orthorectification (Messerli & Grinsted, 2014; Rosenau, Dietrich, & Baessler, 2012). These approaches have improved retrievals of surface displacements in single pairs of images, but computational speed and data availability have limited routine application to larger area mapping (with the notable exception of Rosenau et al. (2012); Rosenau, Scheinert, and Dietrich (2015)).

Here we describe a large area mapping approach that takes advantage of the high radiometric sensitivity of the Landsat 8 Operational Land Imager (OLI) to map ice flow in both outlet glaciers and their inland tributaries in Greenland and Antarctica, and mountain glacier systems in southern Alaska. We use orthorectified imagery freely available from USGS (L1T Landsat data: see earthexplorer.usgs.gov). The approach is applicable to ice caps and glaciers globally, although additional noise can be introduced into the displacement fields via rapidly changing surface conditions, which shorten the trackable displacement intervals, and unresolved topography due to high relief. Our approach is a straightforward extension of normalized cross-correlation as applied in IMCORR, using several enhancements to take advantage of the improved spatial coverage, radiometric and spatial resolution, modern computational and data handling frameworks, and the large number of image pairs available.

2.2. Processing overview

To measure surface displacements between pairs of Landsat 8 OLI panchromatic images (band 8, 15 m pixel resolution) resulting from ice flow, we find peaks in normalized cross-correlation surfaces calculated at integer pixel offsets between image chips. We cross-correlate using a "template" chip of 10–40 pixels on a side (150–600 m on the ground) at integer pixel offsets relative to a larger "source" chip from a later image, fitting the peak of the correlation surface to estimate the chip offset to the sub-pixel level. In this respect, PyCorr takes an identical approach to the IMCORR software package, but is computationally more efficient through use of open-source libraries for cross-correlation (opencv.org) and geospatial transformations of the data (www.gdal.org). Peak correlation value (*corr*), the difference between the peak correlation value and the second highest peak in the correlation surface (*delcorr*), and curvature of the peak in two dimensions are also recorded (*d2x*, *d2y*). These metrics facilitate the recognition of erroneous matches (incorrect peak selection, poorly defined or missing peaks due to noise) and allow for error estimates of each match. These methods are relatively common in cross-correlation image processing, and are discussed more extensively elsewhere (e.g., Pan, Qian, Xie, & Asundi, 2009). Precision of ice flow measurement for a well-correlated single pair is <0.1 pixels; accuracy of ice velocity is dependent on correcting for the geolocation errors in the scene pairs and the separation in time between the two images. Chip size selection is discussed in a subsequent section. Using a conventional current-model desktop single-cpu (six or eight core) computer, we are able to process full Landsat 8 scene pairs in a few minutes. Processing of ~10,600 ice sheet image pairs for the 2013–2014 daylight season in Antarctica required 10 days, comparable to the download times required to assemble the imagery.

2.3. High-pass spatial filtering

To extend velocity measurements into the ice sheet interiors, we modify previously developed filtering techniques to achieve new surface texture tracking capabilities with Landsat 8. The cross-correlation approach to measuring surface displacement requires a common frame of reference between two images, which was difficult to obtain for earlier Landsat imagery that were poorly geolocated (~100–1000 m), and without static features (i.e., exposed bedrock) in the field of view. To address these problems, Scambos et al. (1992) generated high-pass and low-pass filtered versions of the original images, using kilometer-scale filter kernels. The low-pass filtered version of the images isolated quasi-stationary surface undulations resulting from ice flow over bedrock while the high-pass version isolated smaller scale features that are advected with the ice flow. The low-pass filtered images could then be co-registered with normalized cross-correlation, enabling accurate (~±1 to 2 original image pixels) image coregistration even in areas where the entire field of view was flowing. Cross-correlation could then be applied to the high-pass filtered versions to determine the displacement due to ice flow alone. Even with these advances, the radiometric constraints of earlier sensors limited successful displacement retrievals to crevassed surfaces, with few reliable retrievals over the low-contrast ice sheet interiors.

The geolocation knowledge for Landsat 8 OLI imagery is on the order of half a pixel (Storey, Choate, & Lee, 2014) and therefore does not require the same coregistration improvements as earlier sensors. Instead, we apply a high-pass filtering scheme to Landsat 8 solely as a means to isolate the surface features that are advected with ice flow, substantially improving displacement retrievals (Figs. 2 and 3). To do this we high pass filter the original panchromatic band images using a gaussian high pass filter with a ~3 pixel standard deviation (~50 m). The texture visible in the high pass filtered 15-m pixel imagery strongly enhances localized contrast features such as crevassing and sastrugi (Fig. 2). This type of approach was used by de Lange, Luckman, and Murray (2007) to isolate small surface features for motion tracking in SAR imagery.

2.4. Image correlation vs time

Based on the spatial coherence of feature tracking offsets derived in this manner, it is clear that the surface textural patterns visible in OLI band 8 (panchromatic band) high-pass filtered imagery are trackable (correlatable) and persistent. Smooth offset fields for these small-scale surface features across the images show that tracking results are independent of the stationary undulating topography. Initially, we used OLI image pairs with time separations of 16 to 64 days, expecting that small-scale surface features would be modified over longer time separations (i.e. loss of correlation). This was generally true for high-accumulation regions such as the Getz Ice Shelf in Antarctica. However, in low accumulation areas we found that correlatable features can remain with sufficient persistence to track displacement in slow moving, uncrevassed areas, such as the East Antarctic Plateau, for longer time separations.

The persistence of surface texture structures is strongly related to accumulation rate and wind direction variability. In areas such as the Getz Ice Shelf in coastal West Antarctica, and southeastern Greenland, surface texture changes frequently, even within a single 16-day repeat period. However, broad areas of West Antarctica and non-coastal areas of Greenland showed textural persistence and trackable features for >100 days. Areas on the East Antarctic Ice Sheet where katabatic airflow dominates the wind patterns and the accumulation rate is <10 cm water equivalent snow per year showed the most persistent textural patterns, with some areas maintaining correlation for periods longer than a year. In some areas these features slowly evolve into new forms, and we find that correlation degrades with any significant change. The offset between ice flow direction and wind direction (Fig. 2) indicates that sastrugi migration is unlikely to be mistaken for ice flow, and in any case the features do not migrate in concert over ~300 m (image chip) scales.

Fig. 4 shows peak correlation values for a Landsat 8 scene over the Byrd Glacier catchment in East Antarctica for time separations from 32 to 384 days. The first image is common to all of the pairs in the figure. While generally there is a gradual decrease in correlation over the time period, there is a significant drop at 112 days, and some areas that show as high a correlation at 384 days as at 64 days. A detail from the 32 day and 112 day pairs (Fig. 5) shows that near-surface blowing snow obscures surface contrast in the 112 day pair, resulting in poor correlation. Areas devoid of drifting snow show higher correlations

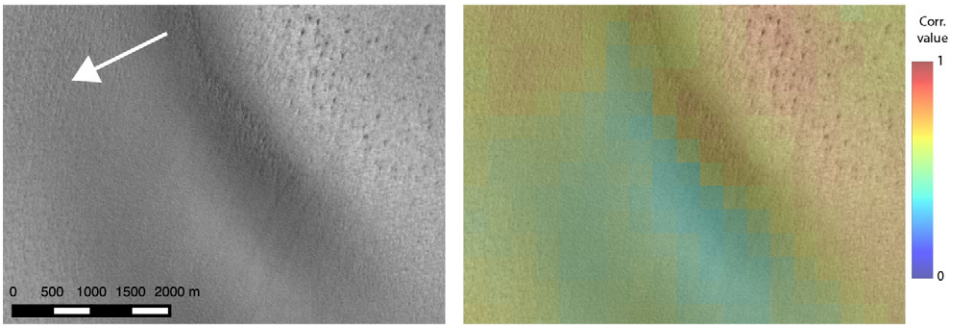

Fig. 2. Left: OLI panchromatic band closeup of surface texture on the East Antarctic Plateau, including large sastrugi and related drift tails (upper right), smooth wind glaze region (center), and smaller-amplitude roughness (left). Solar illumination is from the upper right. The larger topographic feature is an undulation formed by ice flow over the underlying bedrock. Right: Color shows correlation strength for each subscene template chip with the source image used to track motion (Path 54, Row 118: 31 October (background for both panels), and 02 December, 2013). Template chip size is the same as the individual color tiles in this image (300 m). Note high correlation values for all but the smoothest areas of glaze. Arrow indicates approximate ice flow direction; sastrugi texture indicates that the local wind direction is approximately 45° counterclockwise from ice flow.

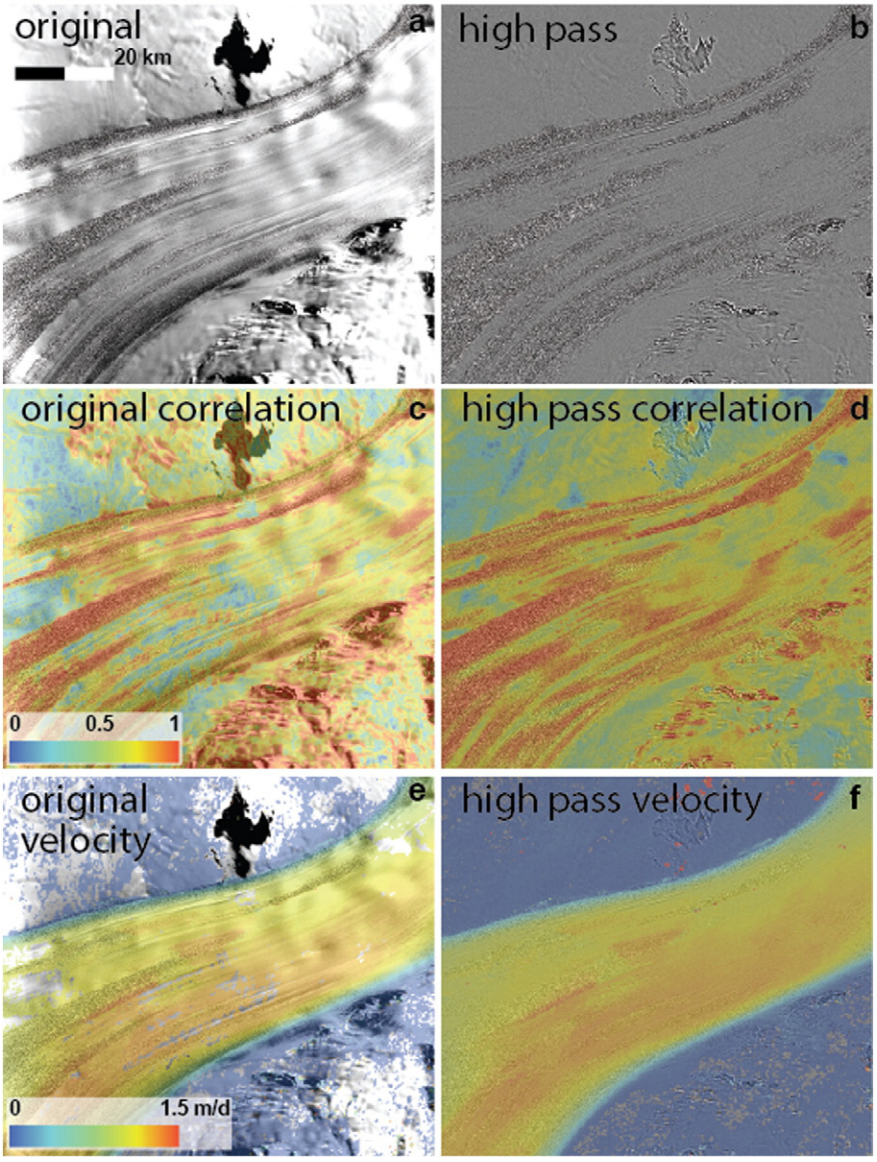

Fig. 3. Effect of high-pass filter processing on Landsat 8 pair velocity extraction (Path 172, Row 118, dates 10 October 2013 and 14 January 2014, Slessor Glacier in East Antarctica). High-pass filtering (b) of Landsat 8 OLI scene (a) leads to enhancement of small-scale features moving with the ice and elimination of kilometer-scale brightness variations from topography related to bedrock structure and ice flow. High-pass filtering produces generally higher correlation index values (d) and more complete ice velocity mapping (f) than the unfiltered scene (c and e).

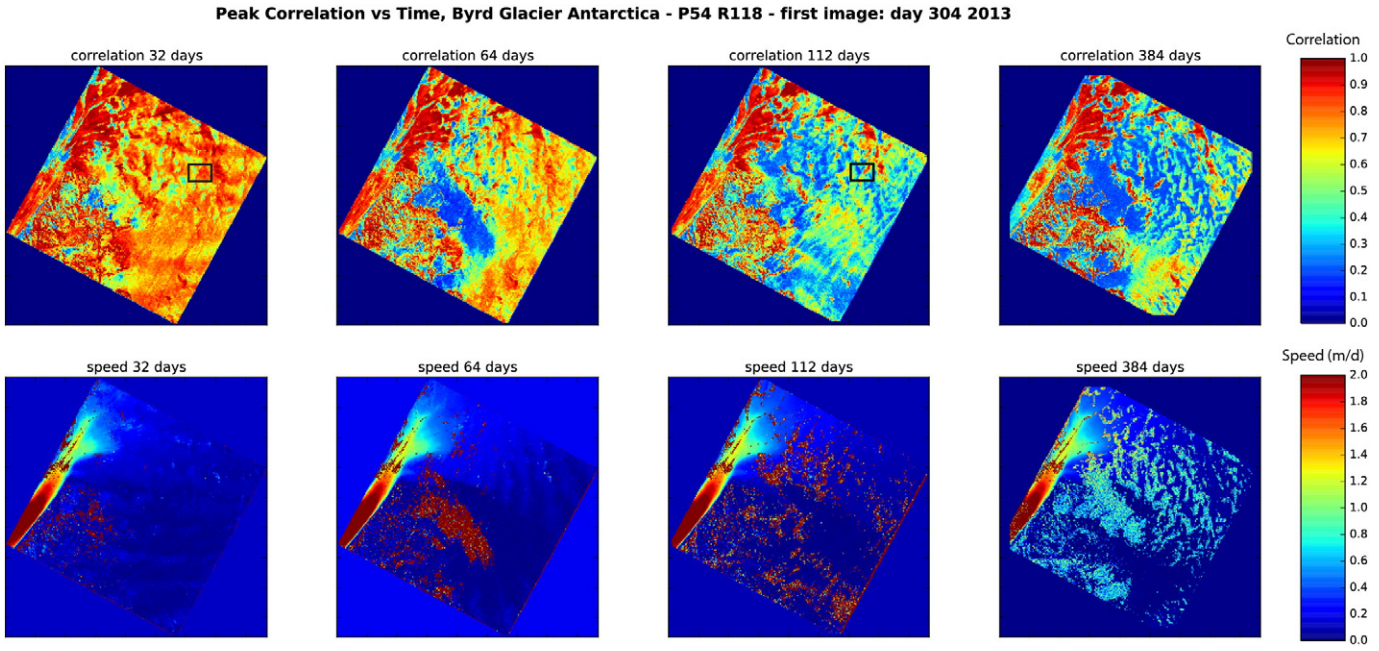

Fig. 4. Top row: Peak correlation values for image pairs with increasing time separation in the Byrd Glacier catchment region of East Antarctica, with time separations of 32 to 382 days. For significant parts of the glacier and surrounding Plateau the correlation is well maintained for more than one year. The lower correlation in the 112-day pair due to blowing snow is shown in detail in Fig. 5. Image chip correlations in uncrevassed areas decrease as the time separation of L8 image pairs increase, but this does not impede an accurate velocity retrieval until correlations drop below ~0.2. Bottom row: Ice flow speed measured over the same intervals, in m/d. Areas of random speckle correspond to low correlation areas; these were not masked here to highlight the loss of correlation and resulting randomness of returned matches. Black boxes in upper right of the 32-day and 112-day panels indicate detail area shown in Fig. 5.

useful for velocity mapping. The fact that the peak correlations remain high in subsequent images demonstrates the persistence of the surface features, even when subject to this type of event (at least for East Antarctica), and shows that moderate levels of blowing snow in very low accumulation areas, even over a year, do not substantially change the surface texture patterns being used for tracking.

2.5. Sub-pixel offset determination

To facilitate accurate displacement measurement, we take advantage of the tendency for ice sheet and glacier images to have a smoothly varying correlation surface in the vicinity of a valid match. We use a bivariate cubic spline to fit the peak in the integer-pixel offset correlation surface, and then find the sub-pixel location of the peak of this spline. For computational efficiency, we perform a maximum gradient search of this splined surface in the gridded x and y directions, locating the peak to within ~0.01 pixel. The resulting offset fields show smoothly varying values, suggesting that the data are not being overfit. Fig. 6a shows the flow speed over Pine Island Glacier in Antarctica, while Fig. 6b shows only the sub-pixel part of calculated offsets. With only the fractional component of the y pixel offset shown, values in this figure wrap at ±0.5 pixels, producing an appearance similar to a differential

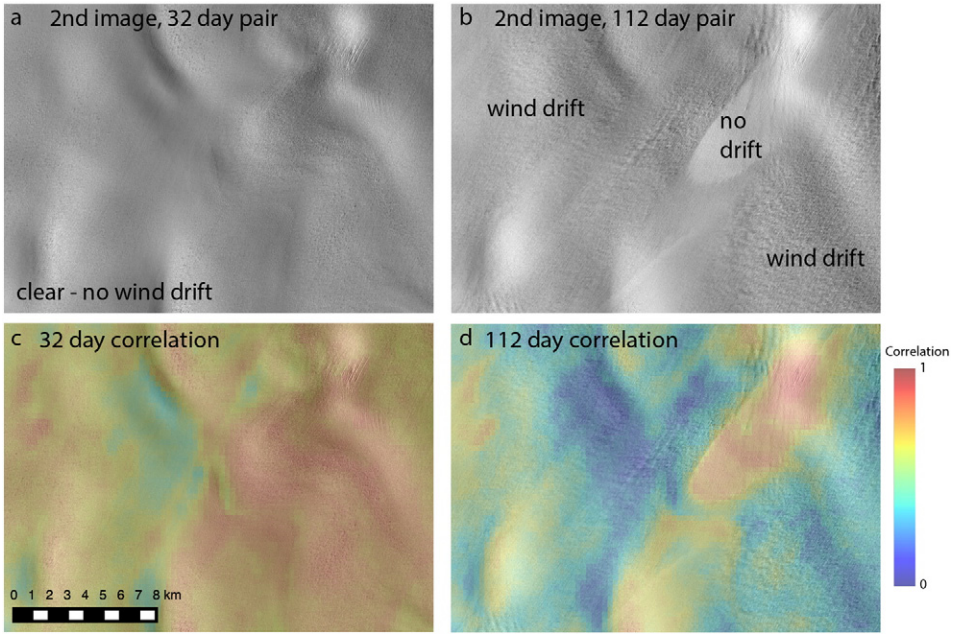

Fig. 5. Detail of the second Landsat 8 image in each pair (top) and correlation values (bottom) for 32-day (left, a and c) and 112-day pairs (right, b and d) from Fig. 4. Sastrugi and longitudinal drifts overlie long wavelength surface undulations in (a); in (b) these are obscured by blowing snow except for clear areas, where correlation values (d) are comparable to those in (a).

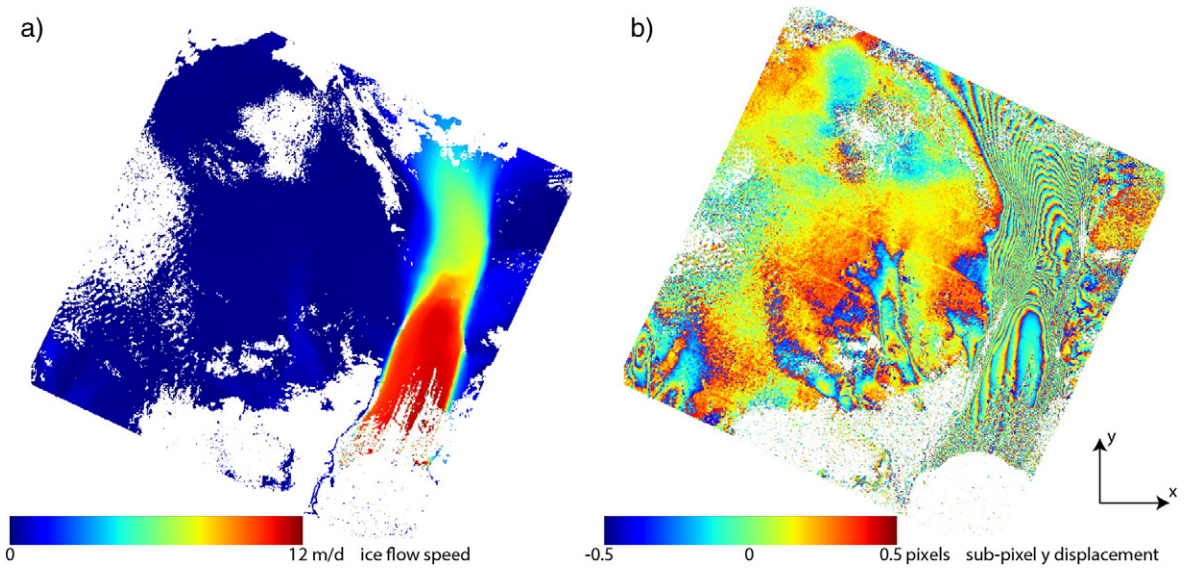

Fig. 6. a: Ice flow speed for a 32-day Landsat 8 OLI band 8 scene pair of Pine Island Glacier, West Antarctica. b: The sub-pixel part of the *y* component (bottom to top in image) of displacement. Color shows the fractional part of the pixel offset determined by fitting the correlation peak as described in the text. The smoothly varying sub-pixel displacement field demonstrates the spatial fidelity of the velocity determinations.

interferogram from Synthetic Aperture Radar (SAR) data. The smoothly varying sub-pixel displacement field, particularly in the slow-moving areas, demonstrates the fidelity of both the internal image geometry and the derived offsets.

2.6. Noise filtering

PyCorr produces pixel displacements at 0.01 pixel increments in the image grid *x* and grid *y* directions which are then converted to output fields of component velocities (md^{-1}; *vx* and *vy*), and speed (*vv*). Results from near-nadir imagery projected into map plane coordinates contain no information about the vertical component of displacement; here horizontal displacement is measured. The *vx*, *vy*, and speed grids are posted at 300 m spacing (i.e., a 20-pixel grid for OLI band 8) representing the mean motion of the correlatable features within a 600 by 600 m patch of glacier surface (40 by 40 pixel template chip) for Antarctic applications. Smaller (20×20 or 10×10 pixels; 300 m or 150 m on a side) template chips are used for outlet glaciers in Greenland and glaciers in Alaska. We filter noise and perform image pair offset corrections on the individual velocity maps before compositing the masked velocities onto a larger grid or combining them into a time series.

We generally mask all doubtful data, because the high number of velocity grids available support extensive or complete mapping even with a conservative approach. We first mask velocities whose *delcorr* value is less than 0.15 (i.e., for which there was a nearly-equal secondary correlation peak at a different displacement). For the remaining unmasked velocities, we examine the difference between speed at the assessed pixel and the 8 adjacent speed values, which may or may not be populated. If the assessed location has no valid velocity neighbors, it is masked. If only one of the 8 neighbor locations is populated, we mask the center pixel if the difference between the two speeds is greater than 1 md^{-1}. With 2 or more neighbors, we take the standard deviation (σ) of the neighbors, and require $\sigma_{min} > 0.01$ md^{-1} and that the center value be within 3σ of the mean of the neighbors, or it is masked (this has the undesired effect of eliminating areas with *identical* speeds in the grid, but this is not often encountered). After this, the overall 3×3 region σ is computed, and the center pixel of each region is masked if $\sigma > 1$ md^{-1}.

2.7. Adjustment of geolocation errors

Despite the improvement in geolocation accuracy with Landsat 8, residual geolocation errors (~3 to 10 m) often remain, introducing an artificial offset between the images in a tracked pair. This is particularly problematic for closely-spaced pairs (16- and 32-day separations) for which the residual geolocation error is a significant fraction of, or larger than, the surface displacement between scenes in slow moving areas. Since most geolocation errors in Landsat 8 present themselves as nearly planar shifts between image pairs, we are able to largely correct for these errors without impeding our ability to detect and accurately map real ice displacement (i.e., from one seasonal compilation to the next) by a simple *x* and *y* shift to bring the displacement field to zero over stationary features. In many areas this can be achieved through identification of exposed bedrock. However, Landsat scenes without outcropping bedrock commonly exist on ice sheets (as discussed earlier; also, Scambos et al., 1992). For those scenes we identify regions that overlap near-zero (<10 ma^{-1}) or slow moving (10–25 ma^{-1}) areas in recent InSAR-based compilations (e.g., Rignot et al., 2011 for Antarctica; Joughin et al., 2010 for Greenland) and apply constant shifts in *x* and *y* to the entire Landsat-derived displacement grid to have these areas approximately match the InSAR results. If >2% of the area of the Landsat velocity mapping overlies the InSAR near-zero flow areas, we apply a correction so that the mean Landsat speed is zero in the overlap. If the near-zero overlap area is less than 2% of the Landsat mapping, we solve for scalar *x* and *y* shifts to apply to the Landsat data such that the mean of all overlapping x and y velocities for slow moving areas match InSAR mappings. No correction is applied if the area covered by velocities <25 ma^{-1} totals less than <2% of the mapped area (the uncorrected velocity grid may or may not be incorporated, depending upon the benefit of coverage versus high accuracy). This approach assumes that slow moving ice experiences small absolute changes in ice speed. The majority of known ice flow speed changes in the ice sheets are occurring near the coasts, in areas of moderate to high flow

speed (e.g., Mouginot, Rignot, & Scheuchl, 2014; Moon, Joughin, Smith, & Howat, 2012; Rignot, 2008; Wuite et al., 2015).

2.8. Reprocessing of Landsat 7 data

Improvements in processing and geolocation of Landsat 7, combined with our ice velocity processing system and additional steps in image enhancement, can improve the past coverage of Landsat 7 derived ice velocity data, supporting an improved change detection comparison with Landsat 8 ice velocity data. Acquisition rates of ice-covered areas for Landsat 7 were typically a third of the present acquisition rate for Landsat 8 (Fig. 1), but during the early Landsat 7 operation, there was a focus on high acquisition for certain ice-covered areas as part of a mosaicking effort (e.g., Landsat Image Map of Antarctica, LIMA, Bindschadler et al., 2008). Landsat 7 spatial resolution is similar to Landsat 8, with 15 m ground-equivalent pixels for the panchromatic band, and 30 m pixels for the visible, near infrared, and short-wave infrared bands (Goward, Masek, Williams, Irons, & Thompson, 2001). However, Landsat 7 radiometric resolution is limited to 8-bit quantization for all bands. Although two gain settings for acquired images permit some improvement at low light levels (Bindschadler et al., 2008), velocity measurements over ice sheets or glaciers have been limited by the lower Landsat 7 radiometric resolution. In addition, Landsat 7 suffered early (May 31, 2003) loss of its scan line corrector, resulting in large data gaps that reduce the utility of the imagery for velocity mapping after this event.

We achieved a major improvement in the spatial coverage of tracking in Landsat 7 image pairs using PyCorr and pre-processing the images using a principal components analysis. This was used earlier (Scambos et al., 1992) but the improvement for Landsat TM, while notable, was still insufficient to support large-area ice sheet mapping. Our approach here was to re-grid the Band 2 (green), Band 3 (red), and Band 4 (near infrared) data to 15 m ground scale, and create a principal component transform of these three bands and Band 8 (panchromatic), that is, a four-channel transformation (executed using floating point values for the output product). The first principal component in this transformation is a noise-reduced, gray-scale-sensitivity-enhanced image at 15 m that has a greatly improved representation of subtle surface texture used for tracking (Fig. 7). While the method improves the spatial extent of valid tracked features (by approximately 3-fold in the Fig. 7 example), the improved radiometry is still inferior to OLI band 8. The realized improvement is approximately the square root of the number of bands used in the PCA times the original radiometry, or 2×2^8 bits, 0–511. The use of 30 m resolution bands and other factors will make the true realized improvement less than this. Nonetheless, this approach supports regional assessments of ice sheet flow changes in high detail, achieving change detection over the (currently) ~12-year time separation (e.g., ~2001–2013–2014; Hulbe, Scambos, Klinger, & Fahnestock, 2015 in review).

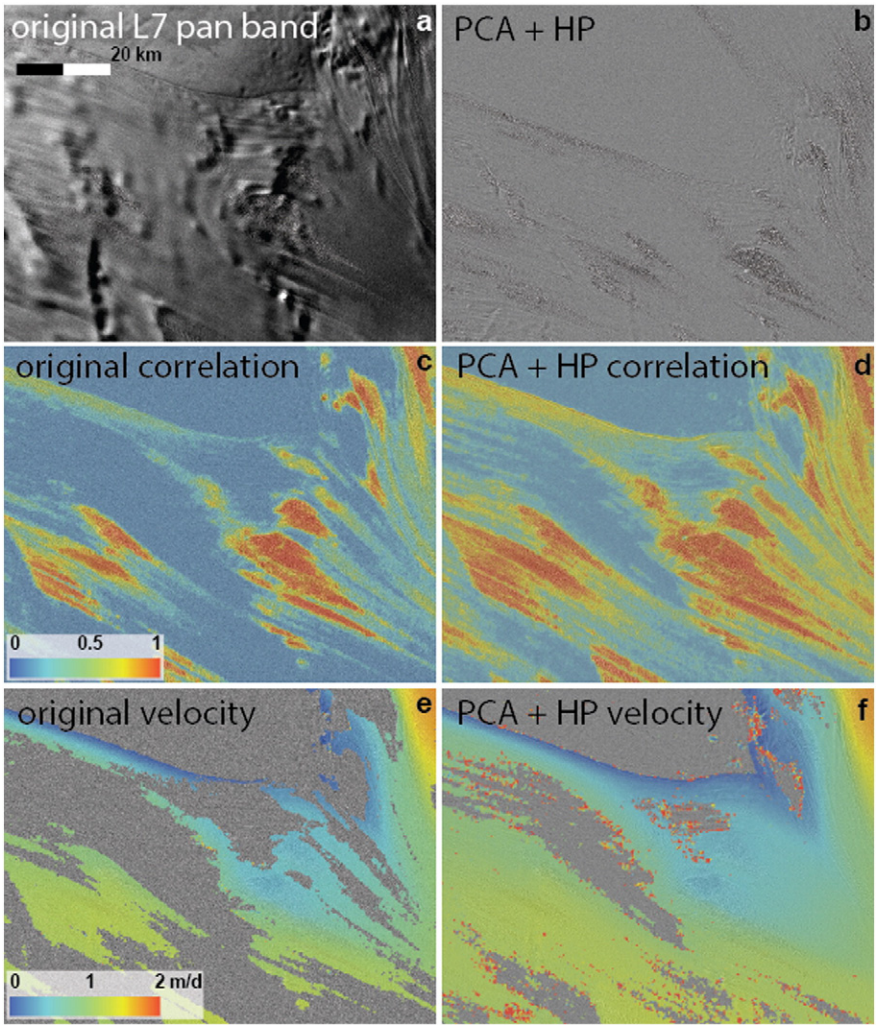

Fig. 7. Illustration of advantage of principal component analysis (PCA) transformation from bands 2, 3, 4, and 8 on a Landsat 7 pair (Path 013, Row 118, 08 Jan. 2001 and 27 Dec. 2001, showing the confluence of MacAyeal and Bindschadler ice streams in West Antarctica). PCA and high-pass filter processing (b) of Landsat 7 image (a) leads to reduced noise and enhanced topographic detail. This process produces generally higher correlation index values (d) and more complete ice velocity mapping (f) than without PCA and high-pass filtering (c and e).

2.9. Applications

Applications for the new velocity data stream created with PyCorr, discussed in this section, take advantage of both spatial and temporal improvements.

2.9.1. Velocity mosaicking of Greenland or Antarctica

After correcting for geolocation errors, the resulting velocity grids (300 m/cell for each Landsat scene) are bilinearly resampled to the target grid spacing. For the target grids, we use the MODIS (Moderate-resolution Imaging Spectroradiometer) Mosaic of Antarctica (MOA) and MODIS Mosaic of Greenland (MOG) (Haran, Bohlander, Scambos, Painter, & Fahnestock, 2014; Scambos, Haran, Fahnestock, Painter, & Bohlander, 2007; see also nsidc.org/data/moa) reference frames. These mosaics have polar-stereographic grids of 125 m and 750 m (MOA) and 100 m and 500 m (MOG). The same noise-filtering algorithm applied to the raw displacement fields is then applied to the resampled fields, but with re-scaled values. For example, for the 750 m MOA grid, the maximum permitted difference between just two values in a 3-by-3 grid is 2.5 md^{-1}; $\sigma_{min} > 0.025$. The standard deviation image resulting from this second masking operation is then passed on to the final compositing algorithm. For other glacier systems we use the Universal Transverse Mercator (UTM) projection of the original Landsat data.

In compositing mosaics of ice velocity (stacking and averaging of collocated ice velocity determinations), we compute a weighting for the individual velocity grids based on the days of separation for each image pair. This reduces the effect of short-interval velocity measurements, which have the highest error, in the final mosaic. For Landsat pairs with 16-day separation, we applied a weight of 0.3 to the output data; for 32-day separation results, weight was set to 0.6; and for 48-day separation it was set to 0.9. For image time separations greater than 48 days, we set the weight to 1.0. In compositing the data, the final weight for each cell is then the weight value based on image pair time-separation (*days_weight*) multiplied by the square root of the correlation (*corr*) for each cell and the square root of *delcorr* for each cell. The weighted average scheme emphasized the best-correlated, longest time-span data, and results in a nearly seamless mapping. Once the weights associated with each velocity measurement are determined, the compositing algorithm used to produce the final mosaic is essentially a weighted averaging, very similar to that described in Scambos et al., 2007.

An example of the ice velocity mosaic product is given in Fig. 8, showing a subsection of a nearly continent-wide mosaic of Antarctica produced from data spanning 01 October 2013 to 31 March 2014. The overall mosaic was built from 10,663 image pairs, of which 7194 were adjusted using near-zero flow speed (<10 ma^{-1}) areas overlap and 867 were adjusted using slow-flow velocities (10 to 25 ma^{-1}) vector adjustment derived from the Rignot et al. (2011) InSAR mapping.

2.9.2. Improved mapping of ice sheet interior flow velocity

The slowest moving interior areas of the large ice sheets (<10 ma^{-1}) remain a challenge to map. InSAR velocity data are susceptible to ionospheric noise, and at very low ice flow speeds this becomes a significant error. The discovery that surface texture on the decameter scale can be tracked in Landsat 8, and that in the highest-elevation, lowest-snowfall areas can be persistent over long intervals (Fig. 4) improves the signal-to-noise ratio for optical image tracking. For example, if tracking accuracy remains at 0.1 pixel (1.5 m) over 1.5 years, then accurate flow direction and speed mapping is possible at 2 to 4 ma^{-1}, if the geolocation error can be removed. To demonstrate this potential, we made a simple composite of the upper Byrd Glacier catchment in East Antarctica from the longest time separation images available at the time of writing, all greater than one year. Fig. 9 shows this composite compared to the Rignot et al. (2011) SAR mosaic of the same area. While patches of the surface have changed too much for correlation tracking, velocities are still recovered for the majority of the area, and compare well with the SAR mosaic speeds. If displacements can be tracked through multiple years, Landsat 8 will be able to provide a more detailed mapping of ice flow than has been possible by any method in the past.

2.9.3. Velocity time series

Understanding processes governing ice sheet mass loss requires studying changes in velocity behavior on both interannual and shorter time scales. Recent research on the Greenland Ice Sheet demonstrates that both land-terminating and marine-terminating areas of the ice sheet display seasonal velocity changes (e.g., Ahlstrøm et al., 2013; Bartholomew et al., 2010; Moon et al., 2014). Seasonal velocity fluctuations can reflect changes in ice discharge and surface meltwater

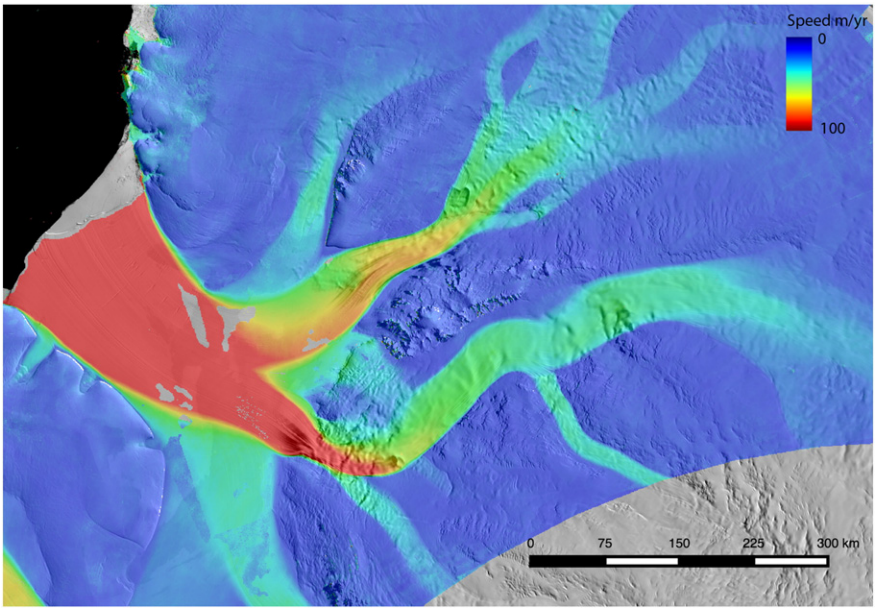

Fig. 8. Ice flow speed from Landsat 8 for the Filchner Ice Shelf and tributary ice streams. Background image is from the MOA2009 image mosaic (Haran et al., 2014). This is a subscene of a continent-wide mapping using 10,663 image pairs spanning the period 01 October 2013 to 31 March, 2014. Velocity data were composited on a 125 m grid (based on the MOA2009 image grid).

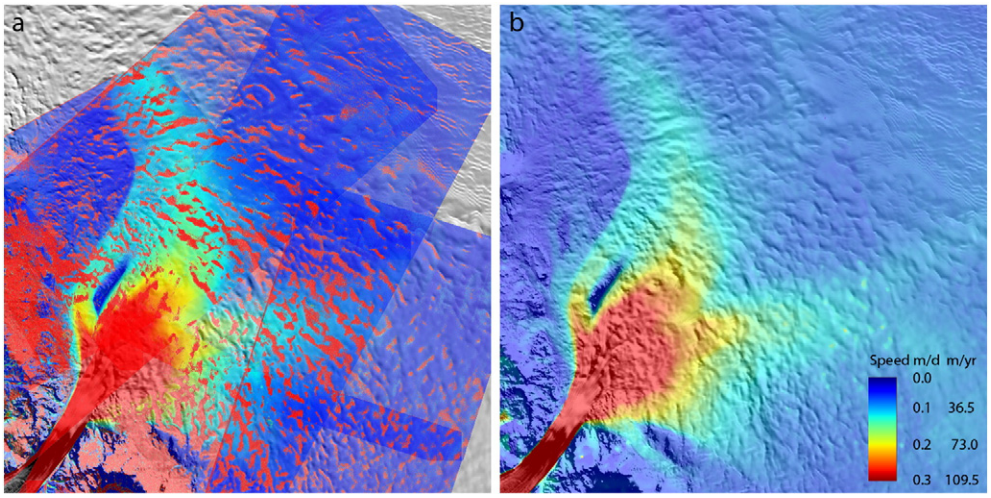

Fig. 9. Large-area mapping of slow moving ice with Landsat 8. a): Ice flow speed of upper Byrd glacier, East Antarctic Plateau, from 8 pairs of OLI band 8 images with time separations ranging from 384 to 432 days. Correlation is well maintained on the plateau except for localized areas of high accumulation on the upwind sides of megadunes and surface undulations (irregular red patches in left panel). Right: InSAR-derived ice flow speed from Rignot et al., 2011. Background image is the 2008–2009 MODIS Mosaic Of Antarctica (MOA2009; nsidc.org/data/NSIDC-0593). Note that the time separations for the Landsat imagery were the maximum available to date for this area from Landsat 8; we expect, based on the spatial coherence of the correlating areas, that future acquisitions will extend the time interval, further improving the signal to noise ratio of velocity measurements in the region.

production, potentially providing a measureable signature of variations in the primary components of ice mass loss, ice discharge and surface mass balance. Being able to measure seasonal ice sheet velocity on an ice-sheet-wide scale, however, has remained a challenge. High temporal resolution point measurements have been made with GPS (e.g., Ahlstrøm et al., 2013; Sole et al., 2011), but require costly fieldwork and are spatially limited. Recent work by Moon et al. (2014) used radar-derived velocity measurements to examine 55 glaciers in northwest, southeast, and southwest Greenland, increasing spatial coverage but with only 3–6 measurements per year for most glaciers. Combining pan-ice-sheet coverage with higher temporal resolution measurements has remained an elusive goal.

The Landsat 8 derived velocities we are now creating with PyCorr provide a substantial step forward for examining seasonal scale time series. Fig. 10 shows an example of five time series extracted along a flow line of Kangiata Nunata Sermia (KNS) in southwest Greenland. By combining measurements over 16 to 64-day separation periods, we produce time series that capture the overall seasonal velocity pattern as it changes from near the terminus to tens of kilometers up-glacier. These data reveal spatial differences in seasonal behavior likely indicative of subglacial hydrologic conditions (Moon et al., 2014). For example, the pronounced late-summer deceleration apparent at the start of the profile line diminishes up-glacier as the amount of melt likely decreases at higher elevations along the KNS flow line. The spatiotemporal coverage possible with our Landsat 8 velocity tracking will enable analysis of

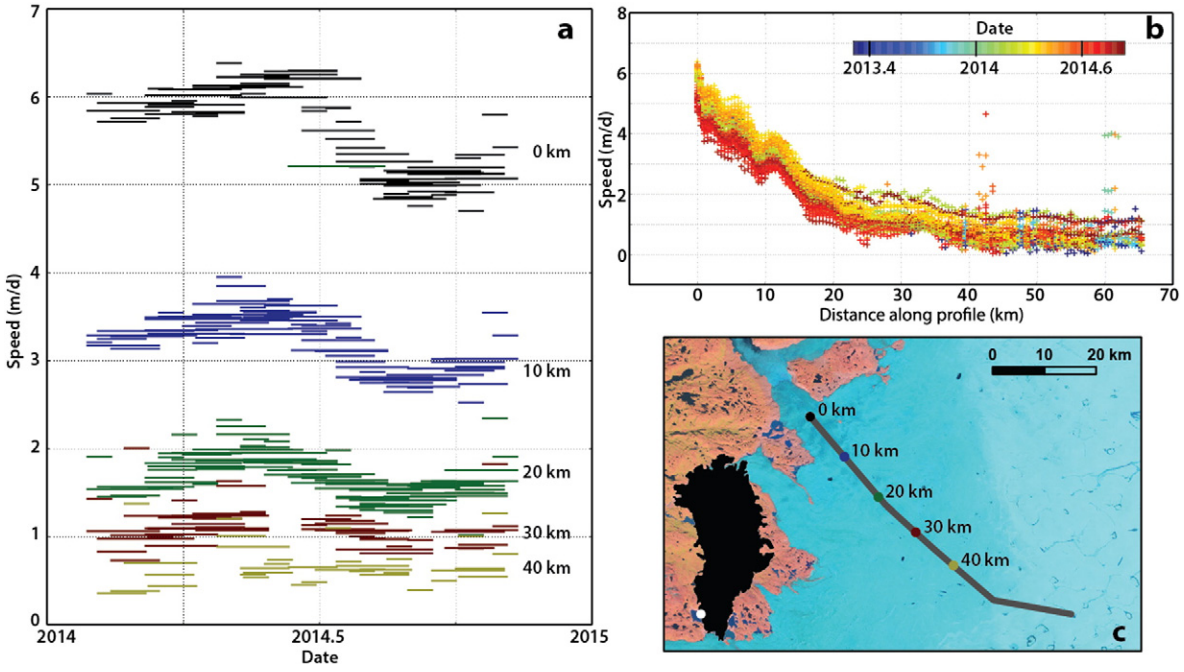

Fig. 10. Landsat 8 velocity measurements for Kangiata Nunata Sermia (KNS), located in southwestern Greenland. a) Velocity measurements at 0–40 km along the ice flow centerline, with length of line indicating image separation time; b) comprehensive plot of centerline velocity from early 2013 through late 2014 (note spurious matches in a few profiles at 42 and 61 km — likely due to lake changes or clouds); c) Landsat 8 false-color image of the area, with sample locations and centerline profile indicated.

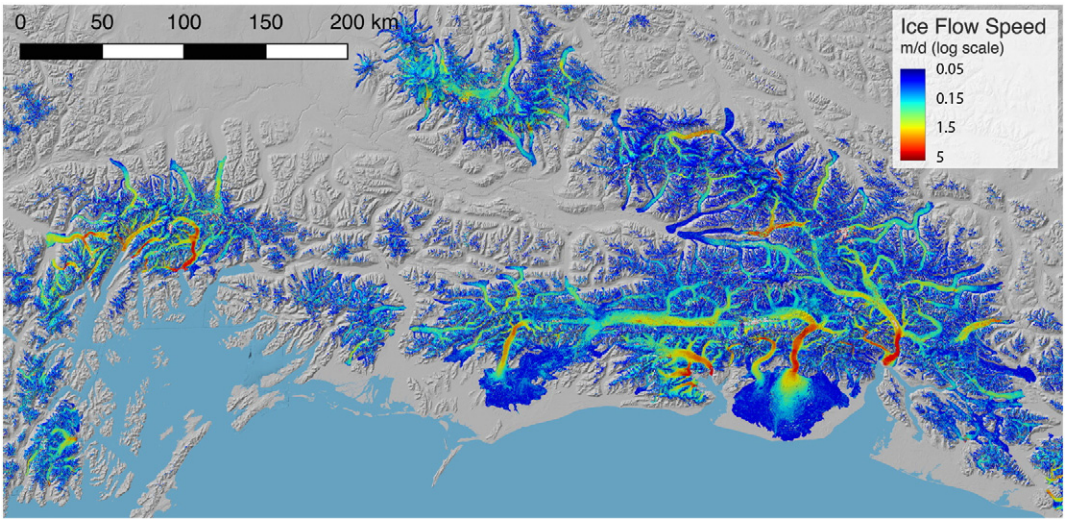

Fig. 11. Mosaic of ice flow speed for the glaciers of southern Alaska, from College Fjord and Columbia Glacier in the west to the Alsek River in the east, with Wrangell-St. Elias in the mid-upper part of the map. This mosaic, posted at 200 m, is composed of trackable Landsat 8 pairs from 2013 to 2015. The coverage is sufficiently sampled in time to develop quarterly (90-day) maps of ice flow speed over the Landsat 8 record for most areas. Base image is a shaded relief from Kienholz, Rich, Arendt, & Hock, 2014; image-pair offset correction used a land mask from Kienholz et al., 2015.

seasonal glacier behavior for all fast flowing (greater than ~200 m/yr) glaciers, with the possible exception of extremely cloudy or low coverage areas (e.g., eastern-most Himalayan glaciers).

2.9.4. Southern Alaska glacier ice speed map

As a last example application, we present a mosaic of the 2014 ice flow speed for much of the glacierized area in southern Alaska (Fig. 11). At this latitude (~61 degrees) most glaciers are captured in three adjacent Landsat paths, providing many opportunities for them to be imaged over the course of a 16-day cycle. While frequent cloud cover is an issue in this area, the time sampling that has been possible over the Landsat 8 period to date allows for similar mosaic coverage on a quarterly basis, showing both seasonal and surge behavior.

3. Conclusions

Leveraging improvements in Landsat 8 radiometric resolution, geolocation accuracy, and acquisition rates, we have developed a processing scheme that enables coastal to interior ice sheet velocity mapping with unprecedented temporal coverage. Our software, PyCorr, provides short processing times, allowing for near-real time velocity mapping from optical imagery. Application to Landsat 7 data, newly reprocessed by USGS, also shows improved velocity mapping. Current applications of these data include developing comprehensive ice sheet velocity mosaics as well as detailed velocity time series, supporting investigations ranging from ice sheet modeling to process studies of outlet glacier dynamics.

With the presented advances in moderate-resolution imaging of the Earth surface and improved image processing software we are now in a position to implement a near-real-time processing system that provides comprehensive ice velocity mapping of global ice cover. Approximately 150 of the ~725 Landsat 8 scenes acquired each day contain glacier ice. Our current processing system is capable of processing over 1000 image pairs per day. Based on this capacity, we are presently working toward implementation of an automated processing and distribution system that would produce edited ice flow vectors for all Landsat 8 data in near real time, using same path-row image pairs with sub-monthly to seasonal time separations. Pending funding, our plan is to implement a near real time archive of these data at the National Snow and Ice Data Center (NSIDC).

Acknowledgments

This work was supported by NASA Grants NNX14AR77G and NNX15AC70G to M. Fahnestock and NNX10Al42G (supplement) to T. Scambos, as well as USGS Contract G12P00066 to T. Scambos (supporting T. Haran and M. Klinger). T. Moon was supported as a Cooperative Institute for Research in Environmental Science (CIRES) Visiting Post-Doctoral Fellow at the University of Colorado, Boulder for July 2014 – June 2015. Funding for A. Gardner's effort was supported by NASA's Cryosphere program. We thank A. Pope for the graphic in Fig. 1, produced using Google Earth Engine.

References

Ahlstrøm, A.P., Andersen, S.B., Andersen, M.L., Machguth, H., Nick, F.M., Joughin, I., ... Box, J.E. (2013). Seasonal velocities of eight major marine-terminating outlet glaciers of the Greenland ice sheet from continuous in situ GPS instrument. *Earth Systen Science Data*, *5*(2). http://dx.doi.org/10.5194/essd-5-277-2013.

Ahn, Y., & Howat, I.M. (2011). Efficient automated glacier surface velocity measurement from repeat images using multi-image/multichip and null exclusion feature tracking. *IEEE Transactions on Geoscience and Remote Sensing*, *49*(8), 2838–2846.

Bartholomew, I., Nienow, P., Mair, D., Hubbard, A., King, M.A., & Sole, A. (2010). Seasonal evolution of subglacial drainage and acceleration in a Greenland outlet glacier. *Nature Geoscience*, *3*(6), 408–411. http://dx.doi.org/10.1038/ngeo863.

Berthier, E., Arnaud, Y., Baratoux, D., Vincent, C., & Rémy, F. (2004). Recent rapid thinning of the "Mer de glace" glacier derived from satellite optical images. *Geophysical Research Letters*, *31*(17). http://dx.doi.org/10.1029/2004GL020706.

Berthier, E., Vadon, H., Baratoux, D., Arnaud, Y., Vincent, C., Feigl, K.L., ... Legrésy, B. (2005). Surface motion of mountain glaciers derived from satellite optical imagery. *Remote Sensing of Environment*, *95*(1), 14–28. http://dx.doi.org/10.1016/j.rse.2004.11.005.

Bindschadler, R.A. (2003). Tracking sub-pixel-scale sastrugi with Advanced Land Imager. *IEEE Transactions on Geoscience and Remote Sensing*, *41*(6), 1373–1377 (EO-1 Special Issue).

Bindschadler, R.A., Fahnestock, M.A., Skvarca, P., & Scambos, T.A. (1994). Surface-velocity field of the northern Larsen ice shelf, Antarctica. *Annals of Glaciology*, *20*(1), 319–326.

Bindschadler, R., Vornberger, P., Blankenship, D., Scambos, T., & Jacobel, R. (1996). Surface velocity and mass balance of ice streams D and E, west Antarctica. *Journal of Glaciology*, *42*(142), 461–475.

Bindschadler, R., Vornberger, P., Fleming, A., Fox, A., Mullins, J., Binnie, D., ... Gorodetzky, D. (2008). The Landsat image mosaic of Antarctica. *Remote Sensing of Environment*, *112*(12), 4214–4226.

Bindschadler, R.A., & Scambos, T.A. (1991). Satellite-image-derived velocity field of an Antarctic ice stream. *Science*, *252*(5003), 242–246.

Debella-Gilo, M., & Kääb, A. (2012). Measurement of surface displacement and deformation of mass movements using least squares matching of repeat high resolution satellite and aerial images. *Remote Sensing*, *4*(1), 43–67.

Emery, W.J., Fowler, C.W., Hawkins, J., & Preller, R.H. (1991). Fram strait satellite image-derived ice motions. *Journal of Geophysical Research: Oceans*, *96*(C3), 4751–4768.

Fahnestock, M.A., Scambos, T.A., & Bindschadler, R.A. (1992). Semi-automated ice velocity determination from satellite imagery. *Eos*, *73*, 493.

Frolich, R.M., & Doake, C.S.M. (1998). Synthetic aperture radar interferometry over rutford ice stream and Carlson inlet, Antarctica. *Journal of Glaciology*, *44*(146), 77–92.
Goward, S.N., Masek, J.G., Williams, D.L., Irons, J.R., & Thompson, R.J. (2001). The Landsat 7 mission: terrestrial research and applications for the 21st century. *Remote Sensing of Environment*, *78*(1), 3–12.
Haran, T., Bohlander, J., Scambos, T., Painter, T., & Fahnestock, M. (2014). *MODIS mosaic of Antarctica 2008–2009 (MOA2009) image map.* Boulder, Colorado USA: National Snow and Ice Data Center. http://dx.doi.org/10.7265/N5KP8037.
Harrison, W.D., Echelmeyer, K.A., Cosgrove, D.M., & Raymond, C.F. (1992). The determination of glacier speed by time-lapse photography under unfavorable conditions. *Journal of Glaciology*, *38*(129), 257–265.
Heid, T., & Kääb, A. (2012). Evaluation of existing image matching methods for deriving glacier surface displacements globally from optical satellite imagery. *Remote Sensing of Environment*, *118*, 339–355.
Hulbe, C., Scambos, T., Klinger, M., & Fahnestock, M. (2015). Flow variability and ongoing margin jumps on Bindschadler and MacAyeal Ice Streams, West Antarctica. *Submitted to Journal of Geophysical Research* (in review).
Jezek, K.C. (2008). The RADARSAT-1 antarctic mapping project. *BPRC Report No. 22*. Columbus, Ohio: Byrd Polar Research Center, The Ohio State University (64 pp.).
Joughin, I., Smith, B.E., Howat, I.M., Scambos, T., & Moon, T. (2010). Greenland flow variability from ice-sheet-wide velocity mapping. *Journal of Glaciology*, *56*(197), 415–430.
Kääb, A. (2002). Monitoring high-mountain terrain deformation from repeated air- and spaceborne optical data: examples using digital aerial imagery and ASTER data. *ISPRS Journal of Photogrammetry and Remote Sensing*, *57*(1–2), 39–52. http://dx.doi.org/10.1016/S0924-2716(02)00114-4.
Kienholz, C., Herreid, S., Rich, J., Arendt, A., Hock, R., & Burgess, E. (2015). Derivation and analysis of a complete modern-date glacier inventory for Alaska and northwest Canada. *Journal of Glaciology*, *61*(227), 403.
Kienholz, C., Rich, J.L., Arendt, A.A., & Hock, R. (2014). A new method for deriving glacier center lines applied to glaciers in Alaska and northwest Canada. *The Cryosphere*, *8*(2), 503–519.
Krimmel, R.M. (1987). Columbia Glacier, Alaska: photogrammetry data set 1981–1982 and 1984–1985. *U.S. Geological Survey Open File Report, 87–219* (pp. 104).
de Lange, R., Luckman, A., & Murray, T. (2007). Improvement of satellite radar feature tracking for ice velocity derivation by spatial frequency filtering. *IEEE Transactions on Geoscience and Remote Sensing*, *45*(7), 2309–2318.
Lindstrom, D., & Tyler, D. (1984). Preliminary results of Pine island and Thwaites glaciers study. *Antarctic Journal of the United States*, *19*(5), 53–55.
Lucchitta, B.K., & Ferguson, H.M. (1986). Antarctica: measuring glacier velocity from satellite images. *Science*, *234*(4780), 1105–1108.
Messerli, A., & Grinsted, A. (2014). Image georectification and feature tracking toolbox: ImGRAFT. *Geoscientific instrumentation, methods and data systems discussions*, *4*(2), 491–513. http://dx.doi.org/10.5194/gid-4-491-2014.
Moon, T., Joughin, I., Smith, B., & Howat, I. (2012). 21st-century evolution of Greenland outlet glacier velocities. *Science*, *336*(6081), 576–578.
Moon, T., Joughin, I., Smith, B., van den Broeke, M.R., van de Berg, W.J., Noël, B., & Usher, M. (2014). Distinct patterns of seasonal Greenland glacier velocity. *Geophysical Research Letters*, *41*, 7209–7216. http://dx.doi.org/10.1002/2014GL061836.
Morfitt, R., Barsi, J., Levy, R., Markham, B., Micijevic, E., Ong, L., ... Vanderwerff, K. (2015). Landsat-8 operational land imager (OLI) radiometric performance on-orbit. *Remote Sensing*, *7*(2), 2208–2237.
Mouginot, J., Rignot, E., & Scheuchl, B. (2014). Sustained increase in ice discharge from the Amundsen sea embayment, west Antarctica, from 1973 to 2013. *Geophysical Research Letters*, *41*(5), 1576–1584.
Pan, B., Qian, K., Xie, H., & Asundi, A. (2009). Two-dimensional digital image correlation for in-plane displacement and strain measurement: a review. *Measurement Science and Technology*, *20*(6), 062001.
Rignot, E. (2008). Changes in west Antarctic ice stream dynamics observed with ALOS PALSAR data. *Geophysical Research Letters*, *35*(12).
Rignot, E., Mouginot, J., & Scheuchl, B. (2011). Ice flow of the Antarctic ice sheet. *Science*, *333*(6048), 1427–1430.
Rosenau, R., Dietrich, R., & Baessler, M. (2012). Temporal flow variations of major outlet glaciers in Greenland using Landsat data. *Geoscience and Remote Sensing Symposium (IGARSS)* (pp. 1557–1560). 2012 IEEE International.
Rosenau, R., Scheinert, M., & Dietrich, R. (2015). A processing system to monitor Greenland outlet glacier velocity variations at decadal and seasonal time scales utilizing the Landsat imagery. *Remote sensing of environment*, *169*, 1–19.
Scambos, T.A., Dutkiewicz, M.J., Wilson, J.C., & Bindschadler, R.A. (1992). Application of image cross-correlation to the measurement of glacier velocity using satellite image data. *Remote sensing of environment*, *42*(3), 177–186.
Scambos, T.A., Echelmeyer, K.A., Fahnestock, M.A., & Bindschadler, R.A. (1994). Development of enhanced ice flow at the southern margin of ice stream D, Antarctica. *Annals of Glaciology*, *20*(1), 313–318.
Scambos, T.A., Haran, T.M., Fahnestock, M.A., Painter, T.H., & Bohlander, J. (2007). MODIS-based mosaic of Antarctica (MOA) data sets: continent-wide surface morphology and snow grain size. *Remote Sensing of Environment*, *111*(2), 242–257.
Sole, A.J.,. D., Mair, W.F., Nienow, P.W., Bartholomew, I.D., King, M.A., Burke, M.J., & Joughin, I. (2011). Seasonal speedup of a Greenland marine-terminating outlet glacier forced by surface melt-induced changes in subglacial hydrology. *Journal of Geophysical Research*, *116*, F03014. http://dx.doi.org/10.1029/2010JF001948.
Storey, J., Choate, M., & Lee, K. (2014). Landsat 8 operational land imager on-orbit geometric calibration and performance. *Remote Sensing*, *6*(11), 11127–11152.
Whillans, I.M., & Bindschadler, R.A. (1988). Mass balance of ice stream B, west Antarctica. *Annals of Glaciology*, *11*(1), 87–193.
Whillans, I.M., & Tseng, Y.H. (1995). Automatic tracking of crevasses on satellite images. *Cold Regions Science and Technology*, *23*(2), 201–214.
Wuite, J., Rott, H., Hetzenecker, M., Floricioiu, D., De Rydt, J., Gudmundsson, G.H., ... Kern, M. (2015). Evolution of surface velocities and ice discharge of Larsen B outlet glaciers from 1995 to 2013. *The Cryosphere*, *9*(3), 957–969.